Schweizerischer Erdbebendienst
Service Sismologique Suisse
Servizio Sismico Svizzero
Swiss Seismological Service

ETH
Eidgenössische Technische Hochschule Zürich
Swiss Federal Institute of Technology Zurich

SITE CHARACTERIZATION REPORT

SLUX: Val Lumnezia (GR)

Dario Chieppa, Franziska Glüer, Mauro Häusler, Donat Fäh

Last Modification: 23rd January, 2022

Schweizerischer Erdbebendienst (SED)
Service Sismologique Suisse
Servizio Sismico Svizzero
Servizi da Terratrembels Svizzer
ETH Zürich

Sonneggstrasse 5
8092 Zürich
Schweiz
dario.chieppa@sed.ethz.ch

Contents

Summary

Val Lumnezia (GR) is a valley in Canton of Grigions south of the village of Ilanz and close to the San Bernardino pass. The valley is generally oriented NE-SW and is crossed by the river Glogn. The area SW of the village of Vignogn was chosen as site for the installation of SLUX seismic station as part of the renewal project of the Swiss Strong Motion Network (SSMNet). In order to better assess the local subsurface, a passive seismic array and a MASW acquisition were performed in August 2021. While the array covers the entire area around the location of SLUX seismic station, the MASW acquisition was performed NE of the installation, along the road.

The results of the horizontal-to-vertical spectral ratio (H/V) show curves with a broad peak, consisting of two smaller peaks, between 2.5 and 5.7 Hz and a trough at about 7.8 Hz. The same trend was identified at two sites at higher frequencies.

The P- and S-wave velocity profiles explore the subsurface down to 250 m and were estimated inverting the results of passive seismic array and MASW acquisition. The velocity profiles in *dinver* have an increasing number of layers (8-14) over the half-space. These models show a thin layer of less than 2 m thickness with shear-wave velocities up to 1000 m/s, a low-velocity zone and another velocity contrast at 50 m. At higher depth, the seismic velocities increase with depth following a linear gradient. The half-space is located between 200 and 233 m depending on the model and does not present a strong increase of velocity.

The results of Neopsy are shown for the best models of Maximum A Posteriori and Maximum Likelihood algorithms. Both models present similar features as the *dinver* profiles in the first 50 m. The main interfaces are at about 16 m, at the end of the first low-velocity zone, and at 50 m. At higher depths the two models present different features: the ML model has a linear gradient with depth and the half-space at 200 m (Vs=3500 m/s), while the MAP model has lower resolution at depth and locate the half-space at about 152 m with Vs=3500 m/s.

The V_{S30} value for the SLUX site is 373.6 m/s, corresponding to soil class B in Eurocode 8 (EC8) and C in Swiss building code (SIA261). The empirical amplification function (ESM) curve for SLUX station predicts an asymmetric peak at 4.65 Hz with amplifications of 4.37. Below 2 Hz and above 7.5 Hz, the ESM curve reaches amplifications close to 1. The theoretical shear-wave transfer functions obtained using the output velocity profiles from *dinver* and Neopsy perfectly overlap between 0.5 and 3 Hz. The *dinver* transfer function has a broad peak at about 4 Hz and two narrow peaks at 11.1 and 18.9 Hz; the Neopsy transfer functions have a narrow peak between 3.9 and 4.3 Hz and several peaks at higher frequency. While the Maximum Likelihood transfer function is similar to the transfer function of *dinver* and to the ESM curve for frequencies above 10 Hz, the Maximum A Posteriori model presents three sharp peaks with amplifications up to 15. To frequencies below 4 Hz, the ESM curve has amplifications lower than the theoretical transfer functions.

1 Introduction

The station SLUX is part of the Swiss Strong Motion Network (SSMNet) and was installed on 16 September 2021, in the framework of the second phase of the Swiss Strong Motion Network (SSMNet) renewal project (Fig. 1). Two sensors were installed at this site: a velocimeter (Lennartz 1 s) and an accelerometer (Episensor). In order to characterize the underground, to estimate the fundamental frequency of the site and the shear wave velocity profile, a passive array measurement and a MASW acquisition were carried out on 10 August 2021.
The site is located around 220 m SE the settlement of Vignogn (GR) on the western side of Lumnezia valley on the active landslide, at an altitude of 1260 m a.s.l.

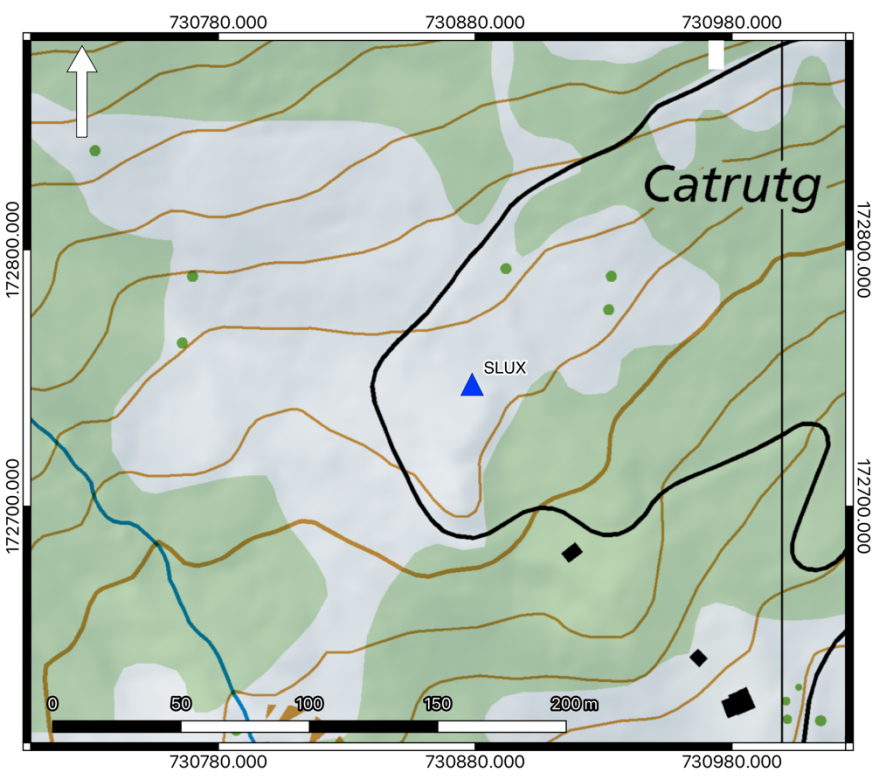

***Figure 1**: Map showing the location of the strong motion station (blue triangle) in Val Lumnezia. Source: Federal Office of Topography.*

2 Geological setting

A geological map of the area SW of the village of Vignogn (GR) and a zoom to the study area is shown in Fig. 2. According to the Geocover map (Source: Federal Office of Topography), the study site is located on a deep-seated and unstable slope that cover the eastern flank of the Mundaun mountain ridge. The landslide, part of the Penninic Scopi zone, has an extension of about 30 km^2 and shows an annual displacement of 1-20 centimeters along a 15 degrees slope. From a geological point of view, the slope consists in coarse sand-quartz and quartzite of Liasic age. Large portions of the slope are covered by moraine deposits (Late Pleistocene).

The surface geology around the SLUX station (blue triangle) consists in fine-grained scree sediments of Quaternary age. The sensors for the passive seismic array (red dots) and the geophones for the MASW line (orange dots) were deployed around the SLUX station on scree sediments.

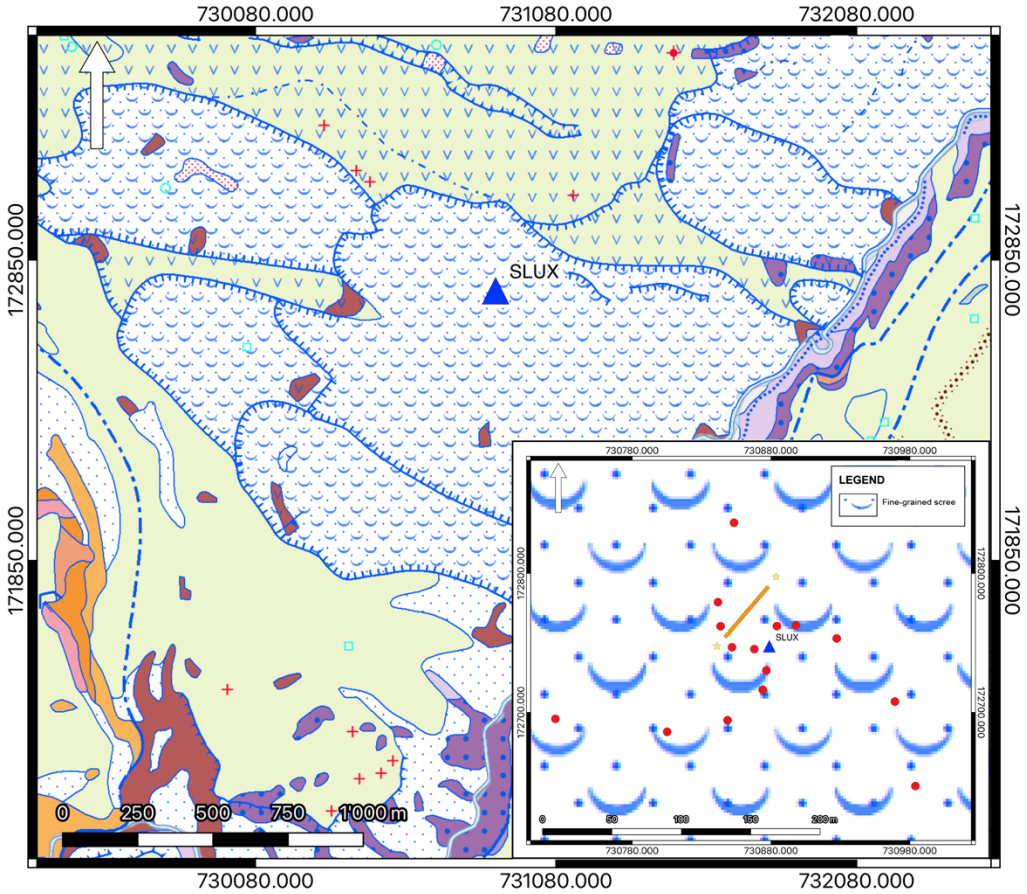

***Figure 2**: Geological map of the surrounding of SLUX seismic station. In the bottom right corner, a zoom of the study area is shown. The strong motion station is represented by the blue triangle, the red dots indicate the locations of the passive array, the orange dots the deployment of 4.5 Hz geophones and the two stars the shot points. Source: Federal Office of Topography.*

3 Active site measurement (MASW)

3.1 Data acquisition

To capture information of the shallow surface, an active seismic acquisition was performed 30 m NW the SLUX installation. A line of 3 times 8 three-component 4.5 Hz geophones was installed parallel to the gravel road. The geophones line is 46 m long with a spacing of 2 m.

The source used for the seismic acquisition consists of a 5 kg sledgehammer and a 25x25 cm metal plate. The acquisition was performed at the two extremities of the geophone line, 10 m from the last geophone. The SW location corresponds to *shot1*, while the other in the NE is *shot2*. At each location, 10 hammer blows were generated. Table 1 summarizes the acquisition parameters.

The recorded data were processed for the multichannel analysis of surface waves (MASW) technique using Matlab routines.

Table 1 Acquisition parameters for the active seismic data.

MASW acquisition parameters	
Spread length	46 m
Receiver spacing	2 m
Source spacing	10 m distance off-spread from first and last geophone
Sampling interval	62.5 ms
Recording length	1.5 s
Pre-trigger delay	0.05 s

Fig. 3 shows the stacked common-source gathers for all three recording components of *shot1* (left) and *shot2* (right). The surface-wave train can be identified for all three components between 0.15 s at 10 offset and about 0.35 s at 56 m offset. For the stacked traces of the vertical component, a near-linear first arrivals with a phase velocity of about 2200 m/s can be observed. The velocities increase with the offset from 2000 m/s to about 2400 m/s at 56 m.

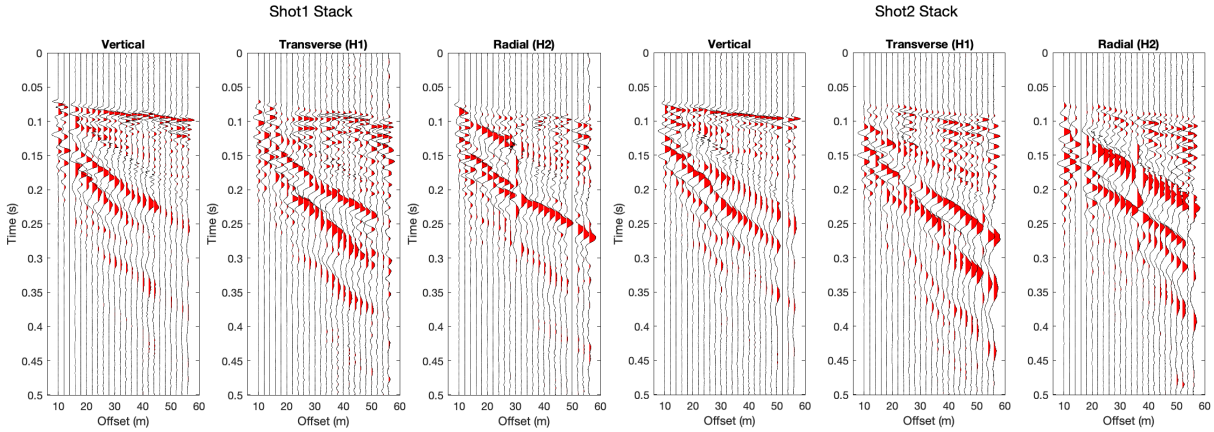

Figure 3: *Left: common-source gather for shot1: vertical, transverse and radial components (trace-normalized). Right: common-source gather for shot2. V: vertical, transverse and radial components (trace-normalized).*

3.2 Data processing

Rayleigh-wave dispersion data were extracted from the vertical and radial components of the seismograms. After removing noisy or dead channels, the remaining traces were processed by 2-D frequency-wavenumber (*f-k*) transform (Socco and Strobbia, 2004) to obtain a conversion of the recorded sets of traces from the time-offset domain to the *f-k* domain. *f-k* panels from single hammer blow records with the same source position were summed to obtain spectral images with greater signal-to-noise ratios. The energy maxima corresponding to the Rayleigh-wave dispersion curves were picked on each stacked panels. Spectral amplitude peaks from individual shot recordings were identified as well and used to define the uncertainty in the estimation of phase velocities (Socco et al., 2009).

Figure 4 shows the stacked *f-k* panels for the vertical and radial components with the picked energy maxima. Top row shows the results for the vertical component for *shot1* (left column) and *shot2* (right column); bottom row shows the results for the radial component for the same two shots.

First inspection of the *f-k* spectra shows significant difference between the two source locations as well vertical and radial components. *shot1* on the vertical component (top left) shows a strong branch up to 35 Hz including wavenumbers up to 0.85 rad/m. Between 13 and 18 Hz, the energy abruptly drops to lower wavenumbers indicating the presence of a dominant higher mode. This phenomenon is more pronounced on the vertical component of *shot2* (top right), where two modes can be distinguished at frequencies higher than 12 Hz. The mode at lower velocities is nearly linear and rather continuous with an increase of energy at 35-38 Hz. The other mode, corresponding to a higher mode is very irregular and discontinuous.

Also, for the radial components, the dispersion curves show substantial differences between *shot1* and *shot2*. In the bottom left plot of Fig. 4 (*shot1*), five branches are observable (5-65 Hz). These are almost parallel and indicate the presence of a fundamental mode and several higher modes. The results for *shot2* (bottom right) present three and not parallel branches whose shape is different from the branches for *shot1*.

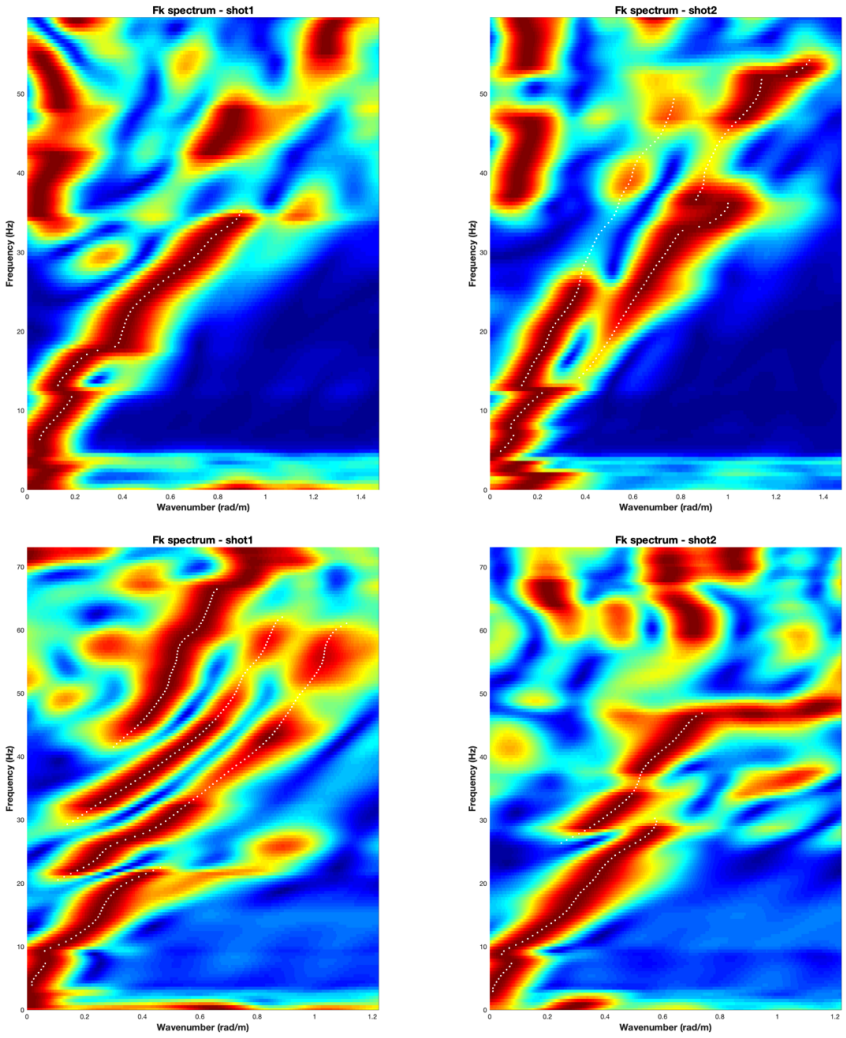

Figure 4*: Stacked normalized f-k spectra obtained from vertical (top) and radial (bottom) components of common-source gathers at source 1 (left column) and source 2 (right column). The source locations were located at 10 m distance from the first and last geophone for source 1 and source 2, respectively. White crosses are picked energy maxima, supposedly corresponding to Rayleigh wave dispersion curve data points.*

Due to the complexity of Rayleigh-wave dispersion curves and the coexistence of several branches, the mode interpretation for the picked modes is provided in Section 5, after the computation of Love- and Rayleigh-wave dispersion curves and the Rayleigh-wave ellipticity curves for the passive seismic array.

4 Passive site characterization measurements

4.1 Data set

To characterize the deep underground structure around the seismic station, a passive seismic measurement was performed in August 2021. The data recorded for the passive seismic array were used for the computation of the H/V curves and dispersion curves.

A single array of 16 stations was installed around the SLUX strong motion station (Fig. 5). The stations were planned to be located on five rings of different radii around a central station

(SLUX101). The three stations of each ring were planned to be 120 degrees one from the other but due to the irregularity of the topography surface, the angles between the stations range between a minimum of 105 degrees in the first ring and a maximum of 136 degrees in the second one. Also, the radii of the rings were subjected to the topography effects and were installed with an average value of 19, 31, 52, 95 and 151 m. The array central station (SLUX101) was located 10 m west of the SLUX installation. Each ring, starting from the second, was rotated with respect to the inner ring of a value ranging between 15 and 29 degrees for the second ring, 12 and 33 degrees for the third ring, 26 and 28 degrees for the fourth ring and between 20 and 24 degrees for the fifth ring. Each station consisted of a Lennartz 5 s sensor connected to a Centaur digitizer, with the exception of three stations in the second ring, which were connected to three stations in the first ring, and one in the fourth ring, which was linked to digitizer in the third ring. These stations had two sensors connected to the same digitizer. The station names are composed of "SLUX" followed by a three-digit number between 101 and 116. The array recording time was 95 minutes (5700 s). The station locations were measured by a differential GPS system (Leica Viva GS10) with a centimeter accuracy. Only at SLUX106 and SLUX115 sites the GPS precision was less accurate with uncertainties of about 50 and 40 cm, respectively.

The seismic traces recorded by the passive array were converted from miniseed to sac, the system response was removed, and the results rotated with respect to the two horizontal components of SLUX101 station. According to the results of the rotation, the installation of the Lennartz sensors suffered orientation problems. Assuming that an error of 10 degrees is normal for the installation of such sensors, the correction that was applied to 11 of the deployed sensors ranges from 15.2 degrees to 173. Only 5 stations had an error lower than 6.5 degrees (SLUX103, SLUX104, SLUX105, SLUX109, and SLUX113). In addition to the orientation problem, as it will be shown in the next paragraphs, the coupling of the metallic tripod with the ground was probably not accurate, thus leading to a loss of information.

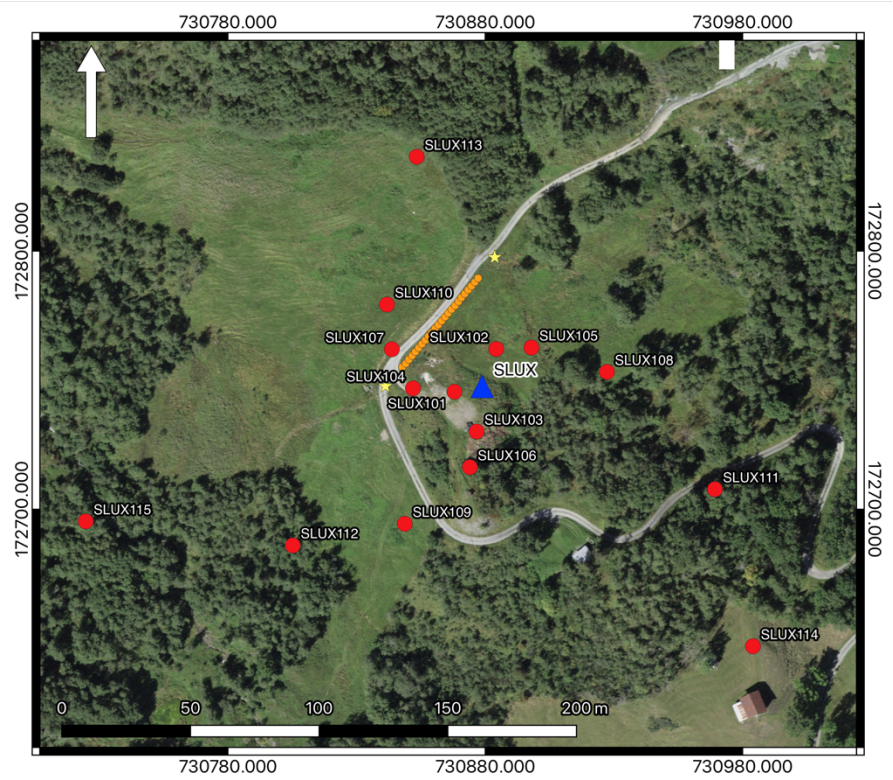

Figure 5*: Layout of the array measurement in Val Lumnezia. The locations of the stations for the passive seismic measurement are indicated by the red dots, the orange dots and the yellow stars represent the geophones and the shot points for the MASW acquisition and the blue triangle indicates the location of the strong motion station SLUX. Source: Federal Office of Topography.*

4.2 H/V and RayDec ellipticity curves

Figure 6 shows the H/V and RayDec curves determined for the sixteen stations of the passive array. The H/V curves are calculated using several techniques. In the left plot of Fig. 6, we show the H/V curves computed using Geopsy software. The H/V curves in the first three rings have a broad peak (2.5-5.7 Hz) and a deep trough (around 7.8 Hz). SLUX112 and SLUX113 show a similar pattern with a narrower peak and a trough that is shifted at higher frequency when compared to the H/V curves in the inner rings. The remaining stations (SLUX107, SLUX110, SLUX111 and SLUX115) have much higher amplitude values and do not have any significant pattern. At low frequency, below 2.5 Hz, all H/V curves diverge. This effect is probably due to the installation and to the coupling of metallic tripods with the ground.

Fig. 7 shows the areal distribution of the H/V peak for the sites of the array. The frequency of the H/V peak is around 3.75-4 Hz at the center of the array and increase up to 7.96 Hz towards north and 5.96 Hz towards SW where the thickness of the sediments cover gets thinner.

The RayDec technique (Hobiger et al., 2009) is meant to eliminate the contributions of other wave types than Rayleigh waves and give a better estimate of the ellipticity. The RayDec results are shown in the right plot of Fig. 6 for all stations of the array. The ellipticity curves show a pattern which is similar to the curves obtained through the H/V analysis: a broad peak at 3-4 Hz and a trough at 8 Hz. At low frequency the pattern due to the bad coupling of the sensors can be seen also for the ellipticity curves, at all sites. The dark green curve indicates the RayDec ellipticity

curve for the array central station, west of SLUX station. This shows an asymmetric peak with a left long flank, a rather broad peak and a steep flank at high frequency. To the right of the peak, a narrow trough and a second broad peak can be identified.

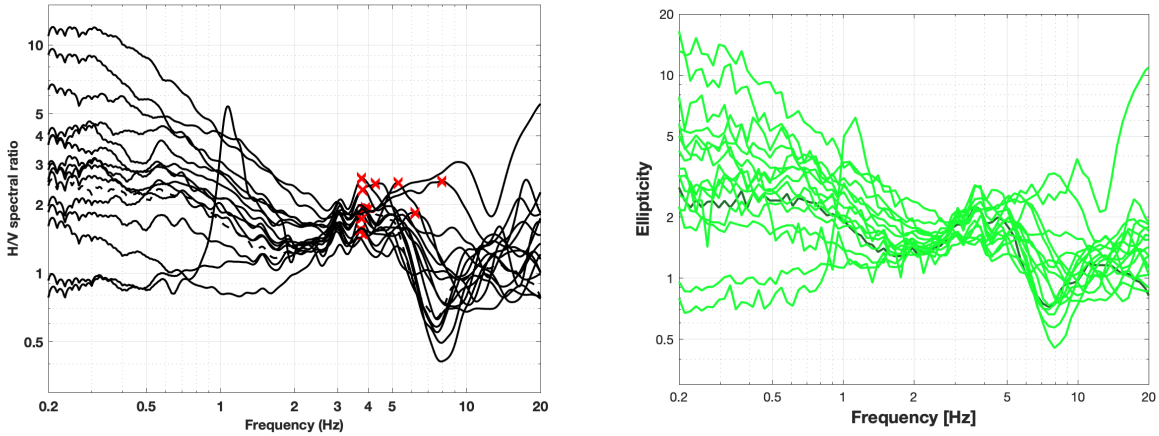

***Figure 6**: Left: H/V curves of the different stations of the array measurements in Val Lumnezia. The red crosses represent the picked fundamental frequency; the dashed curve represents the H/V curve for SLUX 101, the array center. Right: RayDec ellipticities for all stations of the array. The curve for SLUX101 is represented with dashed style (left) or highlighted in dark green (right).*

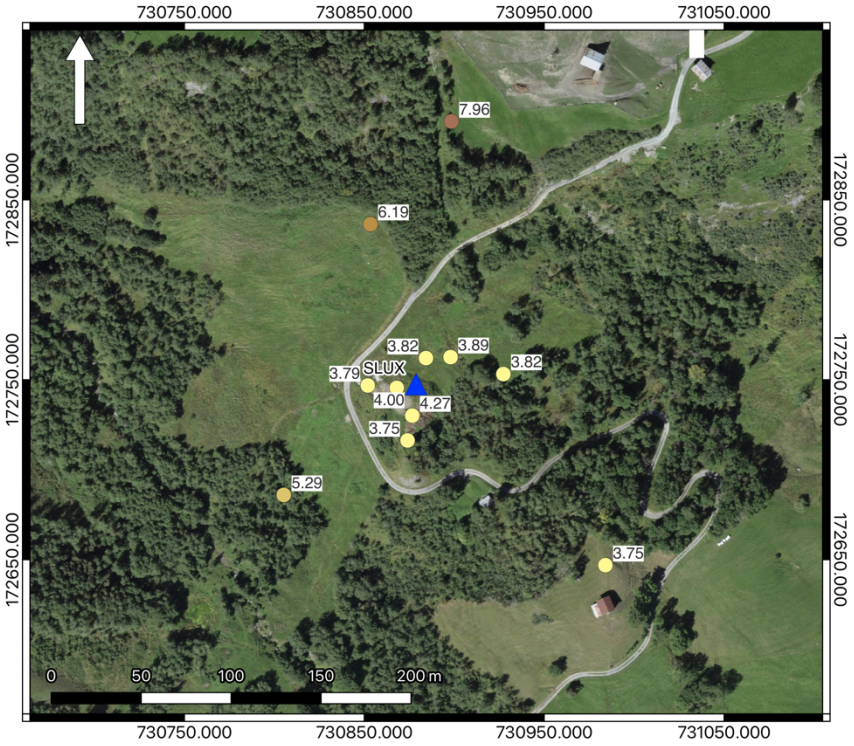

***Figure 7**: Map showing the variation in frequency for the H/V fundamental peak over the area of Val Lumnezia. Source: Federal Office of Topography.*

4.3 Polarization measurements

The polarization analysis was performed according to Burjánek et al. (2010) and Burjánek et al. (2012). The ground motion for SLUX101 station is shown in Fig. 8. Left plot shows the elliptical ground motion over a wide frequency range, up to 30 Hz. This changes to a more linear one around the H/V peak (3-4 Hz) and below 1 Hz. Two directions of polarization can be seen in the right plot of Fig. 8: NE-SW, below 0.1 Hz, and NW-SE around 3-4 Hz. According to the results at other array sites, these directions of polarization are not consistent over the study area.

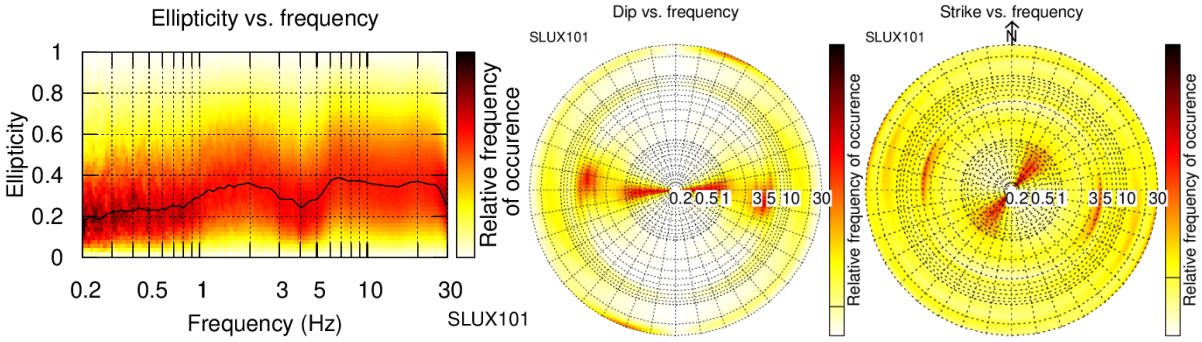

***Figure 8**: Polarization analysis of station SLUX101.*

4.4 3-component high-resolution FK

The results of the 3-component high-resolution FK analysis (Poggi and Fäh, 2010) are shown in Figs. 9 and 10. Fig. 9 reports, from left to right, the dispersion curves computed for the transverse, vertical and radial components. Fig. 10 displays the Rayleigh-wave ellipticity curves for the vertical (left) and radial (center and left) components over the same frequency range as the picked dispersion curves.

Using the transverse component, the Love-wave dispersion curve was picked between 3.18 and 6.94 Hz. The picked curve presents a straight pattern with a small interruption at 5 Hz. The results for the vertical component show a dispersion curve between 4.49 and 8.80 Hz. In the same plot, between 300 and 400 m/s, a rather continuous and energetic alignment takes place over the entire frequency range. It is probably a processing effect and might affect the picking of the dispersion curve. For what concerns the radial component, two dispersion curves were picked: one between 3.55 and 6.82 Hz and the other from 11.77 to 28.67 Hz. The first curve is well defined and has a shape which is similar to the curve picked for the vertical; the other is more difficult to recognize and has shear-wave velocities lower than 400 m/s.

The Rayleigh-wave ellipticity curves were picked according to the frequency range of the picked dispersion curves and are shown in Fig. 10. The curves at low frequency for the vertical and radial components show an opposite trend: the first dips towards high frequency and it is straight, while the other dips towards low frequency and present a small peak at around 6 Hz. Also the ellipticity values of these two curves are different. The ellipticity curve at high frequency for the radial component is flat and has an ellipticity value around 2.

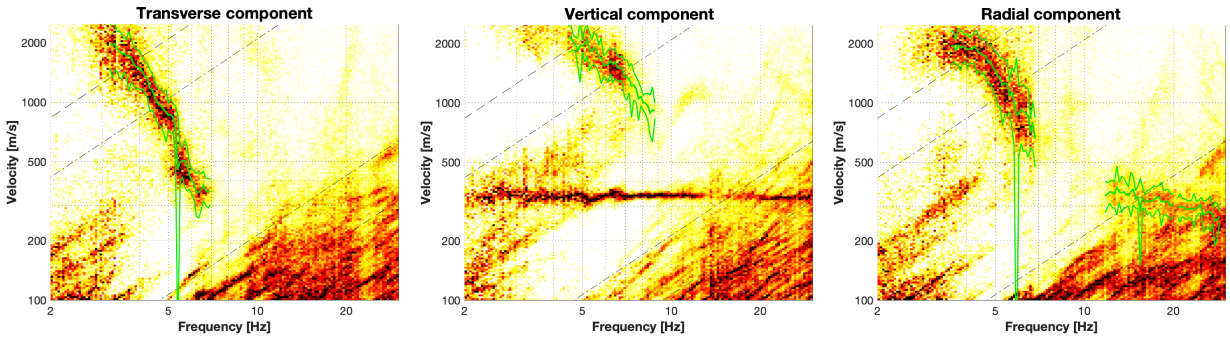

***Figure 9**: Dispersion curves for the transverse (left), vertical (center) and radial (left) components obtained with the 3-component HRFK algorithm (Poggi and Fäh, 2010). The dashed and dotted black lines are the array resolution limits. The solid and dashed green lines represent the data picking (central line) and the standard deviation (outer lines).*

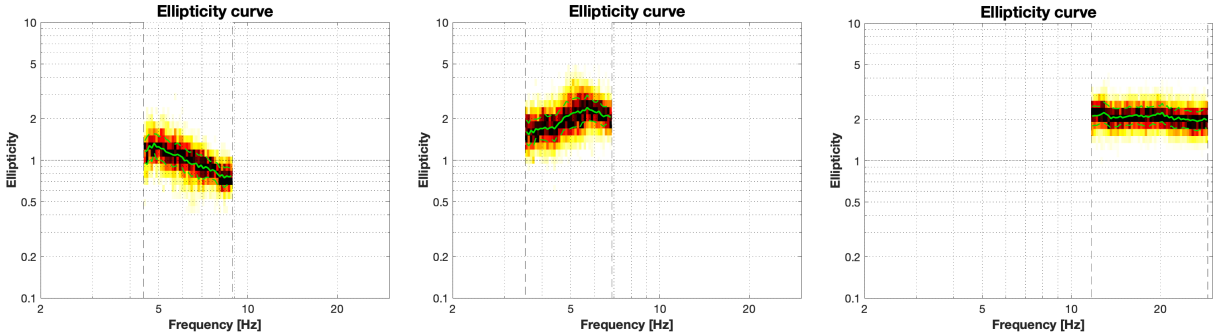

***Figure 10**: Ellipticity curves for the vertical (left) and radial (center and left) components obtained with the 3-component HRFK algorithm (Poggi and Fäh, 2010) over the same frequency range as the dispersion curves picked in Fig. 9. The dashed lines delimit the frequency range of the picked dispersion curves. The solid and dashed green lines represent the data picking (central line) and the standard deviation (outer lines).*

4.5 WaveDec

The results of the WaveDec (Maranò et al., 2012) processing are shown in Fig. 11. This technique estimates the properties of single or multiple waves simultaneously with a maximum likelihood approach. In order to get good results, the parameter γ must be tuned to modify the sharpness of the wave property estimation between purely maximum likelihood estimation and a Bayesian Information Criterion. Here, a value of $\gamma = 0.1$ was used, corresponding to an almost pure Maximum Likelihood estimation.

The results of WaveDec analysis allowed the picking of dispersion and ellipticity angle curves. The dispersion curves were picked in the frequency-wavenumber domain and show one curve for the Rayleigh waves picked between 3.40 and 8.84 Hz and one for the Love waves from 3.40 and 7.34 Hz. The results of dispersion curves are shown in the left column of Fig. 11, top and bottom respectively. Over the same frequency range as the mode picked for the Rayleigh waves, the Rayleigh-wave ellipticity angle curve was picked (top right plot, Fig. 11). Up to 8 Hz, the ellipticity angle values are positive corresponding to a particle motion which is prograde. The ellipticity angle values decrease to zero at 8.1 Hz.

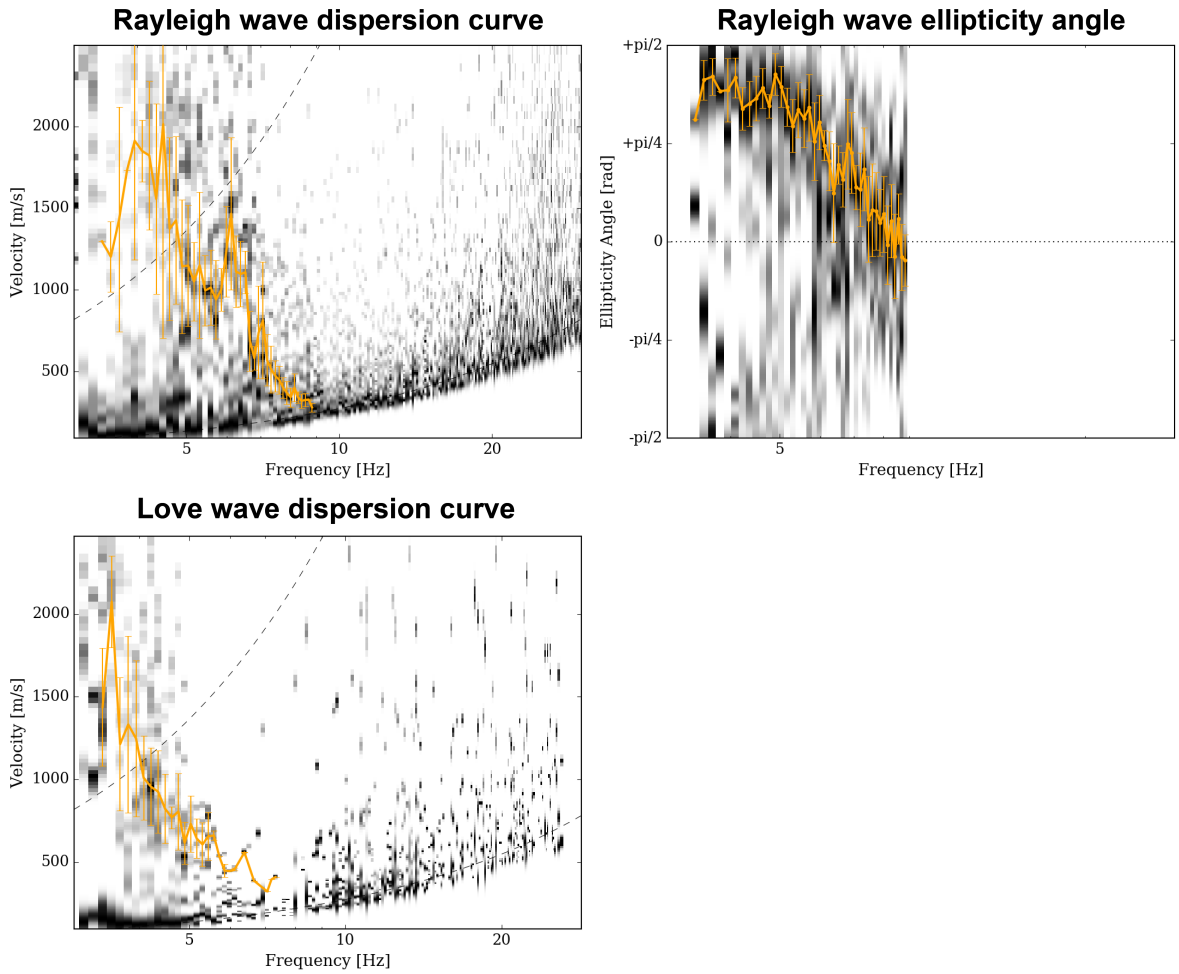

***Figure 11**: Dispersion and ellipticity curves for Rayleigh waves (top row), respectively, and Love wave dispersion curve (bottom row) as obtained with WaveDec (Maranò et al., 2012). The dashed black lines (top rows) represent the array resolution limits, the solid orange line indicates the picked curve and the vertical bars at each frequency show the standard deviation for the ellipticity angle curves.*

4.6 Modified SPatial AutoCorrelation

The SPAC (Aki, 1957) curves of the vertical component have been calculated using the MSPAC (Bettig et al., 2001) technique implemented in Geopsy (Wathelet et al. 2020). Rings with different radius ranges are defined and for all stations pairs with distances inside this radius range, the cross-correlation is calculated in different frequency ranges. These cross-correlation curves are averaged for all station pairs of the respective ring and give the SPAC curves. The rings are defined in such a way that at least three station pairs contribute and that their connecting vectors have a good directional coverage.

Using the results obtained by the SPAC technique and the information collected by the other two array processing techniques, one dispersion curve was picked for the Rayleigh waves between 2.76 and 8.21 Hz. The curve, shown in dark grey curve in the left plot of Fig. 12, presents a rather flat portion below 5 Hz and a much steeper segment at higher frequencies. Central and right plots show the SPAC Autocorrelation curves for the selected rings. The shape of these curves, which should

look like a Bessel function, is related to the geometry of the deployed array and to the difficulties related to the topography, as in this case. The black points in the plots of the second and third columns indicate the data values which contributed to the final dispersion curve estimation and were picked using *spac2disp* tool of geopsy.

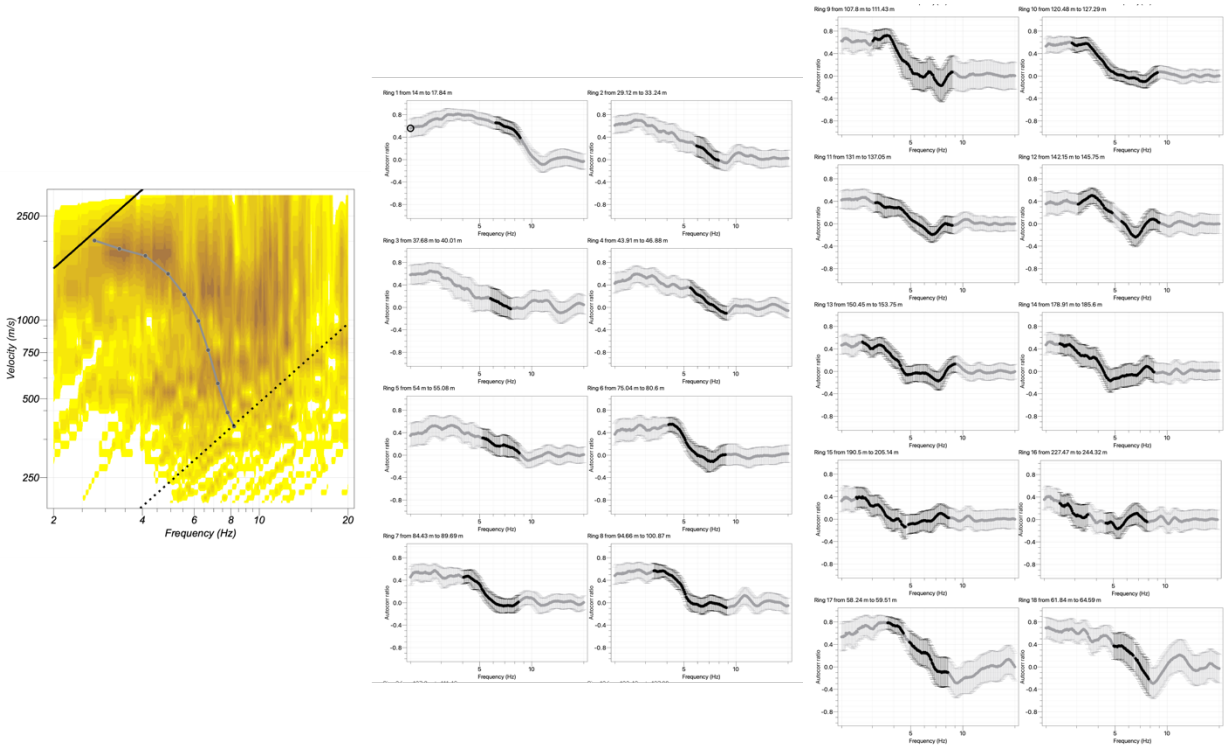

***Figure 12**: Rayleigh wave dispersion curve (left) obtained using spac2disp module of geopsy and autocorrelation functions for all rings (center and right). The solid gray line represents the picked data; the black dashed and dotted lines indicate the array resolution limits.*

4.7 Summary

Figure 13 gives an overview of the Love- and Rayleigh-wave dispersion (left and central plots, respectively) and of the Rayleigh-wave ellipticity curves (right plot) determined using different approaches developed for the analysis of seismic data acquired using active and passive arrays. For Love waves, WaveDec and HRFK techniques produce similar dispersion curves stretching between 3.18 and 6.95 Hz. For the Rayleigh waves, a good agreement can be seen for the curve of WaveDec, MSPAC and the mode at low frequency for the radial component of 3C-HRFK. The mode picked using the vertical component of HRFK (4.6 – 8.8 Hz) show a shape which is similar to the other modes but shifted at higher S-wave velocities. The results of MASW processing are shown using black/grey dotted curves for the radial component (*shot1* and *shot2*, respectively) and dark/light green dotted curves for the vertical component (*shot1* and *shot2*, respectively).
At low frequency, between 2.93 and 7.32 Hz, the MASW curves for the radial component match the mode at low frequency obtained by MSPAC and WaveDec techniques; at high frequencies (9.2-20 Hz) these two curves with similar shapes and similar shear-wave velocities diverges to about 380 m/s at 20 Hz. At higher frequencies and higher S-wave velocities, the black dotted

curves show three branches; the curve for the shot2 was located between two black dotted curves. The dispersion curves for the vertical component of MASW show different behaviors: a segment between 7.32 and 12.21 Hz that connects the mode picked by HRFK (radial), MSPAC and WaveDec techniques with the branch at high frequency for the radial component of HRFK technique. The dark green dotted curve overlaps with the curve at high frequency for the radial component of HRFK for frequencies above Hz. Two almost parallel and horizontal curves in light green colors cross all modes and do not fit all the other picked curves.
The ellipticity curves retrieved using the different methods are shown in the right plot of Fig. 13. The RayDec curve for the center of the array (SLUX101) is plotted in dark green color; it presents a flat portion (0.2-0.8 Hz), three wide troughs and two peaks. The ellipticity curves for the vertical and radial components of HRFK technique are reported in black and red colors, respectively. The ellipticity curve for the vertical component overlaps with the RayDec curve; the other two curves present different trends and values. The ellipticity angle for the WaveDec technique, here converted to ellipticity curve, show a broad peak and a steep flank. This curve is in agreement with the peak for the RayDec curve at about 5-7 Hz and with the right flank up to 8 Hz.

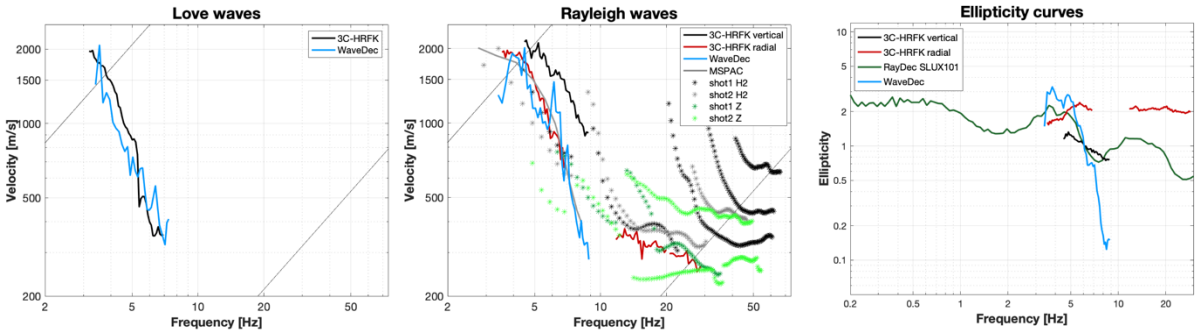

***Figure 13**: Comparison between the computed Love- (left) and Rayleigh- (center) wave dispersion curves and Rayleigh-wave ellipticity curves (right).*

5 Data inversion

5.1 Inversion targets

To define the targets for the inversion, several inversions were performed combining an increasing amount of information.
In a preliminary inversion, the Love- and Rayleigh-wave dispersion curves and the Rayleigh-wave ellipticity angle curve for the WaveDec technique were inverted. The parametrizations tested for this preliminary analysis present a low velocity zone in the shallowest layers (20 m) and an increasing investigation depth: 250 m, 400 m, 600 m and 800 m. According to the results of the inversion and the shape of synthetic dispersion curves, we were able to attribute a mode name to most of the remaining dispersion curves.
The final interpretation is shown in Fig. 14 for the Love- and Rayleigh-wave dispersion curves and for the ellipticity curves. The details of the inversion targets are indicated in Table 2. The fundamental mode of Love-wave dispersion curve is computed using the WaveDec technique and matches the curve used in the preliminary inversion (3.4-7.3 Hz). Three dispersion curves were defined for the Rayleigh waves: one fundamental mode and two higher modes. The fundamental mode is a mix of two curves: the dispersion curve for the WaveDec technique (3.4-8.8 Hz) and the

MASW results for the vertical component (*shot2*) in the frequency range 14.2-32.2 Hz. The first higher mode consists in the 3C-HRFK for the vertical component (4.5-8.8) and several segments of the MASW dispersion curves for the vertical and radial components (13.2-50.3 Hz). The second higher mode corresponds to the dispersion curve for the radial component in the MASW analysis (*shot1*): 22.5-59.6 Hz. Finally, one curve was selected for the Rayleigh-wave ellipticity; this corresponds to the mode picked using WaveDec technique (3.4-8.8 Hz) and it is interpreted as fundamental mode.
An additional test was performed changing the mode attribution for the first higher mode of Rayleigh waves. The curve was selected according to the picking performed for the radial component picked for MASW technique (*shot1*) up to 20 Hz. The results of this analysis were performed using *dinver* and Neopsy techniques and give results similar to the inversions shown in the next paragraphs.

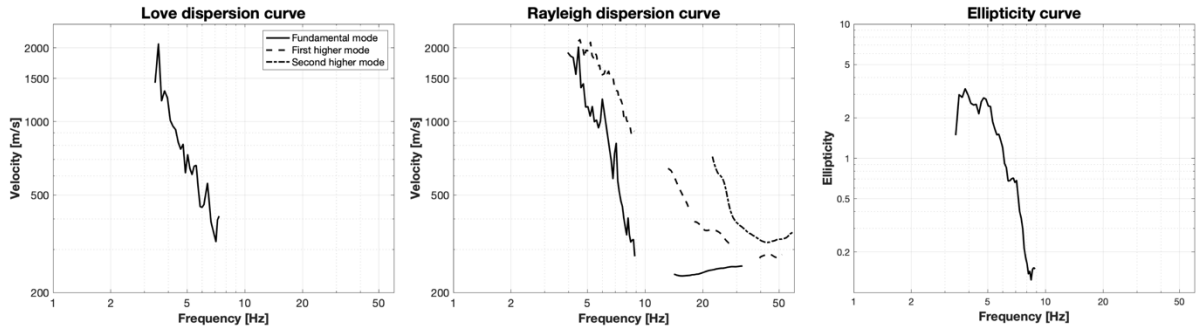

***Figure 14**: Overview of the dispersion (left and center) and ellipticity (right) curves used as target for the different inversions.*

Table 2: List of the curves used as target in the inversion.

Method	Wave type	Mode	Curve type	Frequency range [Hz]
WaveDec	Love	fundamental	dispersion	3.4-7.3
WaveDec + MASW(ver)	Rayleigh	fundamental	dispersion	3.4-8.8 + 14.2-32.2
HRFK + MASW(rad)	Rayleigh	first	dispersion	4.5-8.8 + 9.77-20.5
MASW(rad)	Rayleigh	second	dispersion	22.5-59.6
WaveDec	Rayleigh	fundamental	ellipticity	3.4-8.8

5.2 Inversion parameterization

For the inversion, five different parameterizations were tested. The first four involve free values of thickness and velocities for the different layers, ranging from 8 to 14 layers over the half-space. The S- and P-wave velocities are allowed to range from 50 to 3500 m/s and from 100 to 7500 m/s, respectively. The deepest layer interfaces were allowed to range to a depth of 250 m for all parameterizations. The density was fixed to 2500 kg/m^3 for the bedrock layer and to 2000 kg/m^3 for all the other layers.
The last parametrization has fixed layer thicknesses and consists of 22 layers over the half-space, with the deepest interface at 250 m depth. Equal ranges were defined for the P- and S-wave velocities and density.

5.3 Inversion results

We performed 5 inversions with different parameterizations (see Table 2) using the *dinver* routine (http://www.geopsy.org/). Each inversion run produced 280000 models in totals in order to assure a good convergence of the solution. The results of these inversions are shown in Figs. 15 – 19.

Table 3: List of inversions

Inversion	Number of layers	Number of models	Minimum misfit
SLUX 8l	8	280000	0.809
SLUX 10l	10	280000	0.673
SLUX 12l	12	280000	0.655
SLUX 14l	14	280000	0.660
SLUX fix	22	280000	0.707

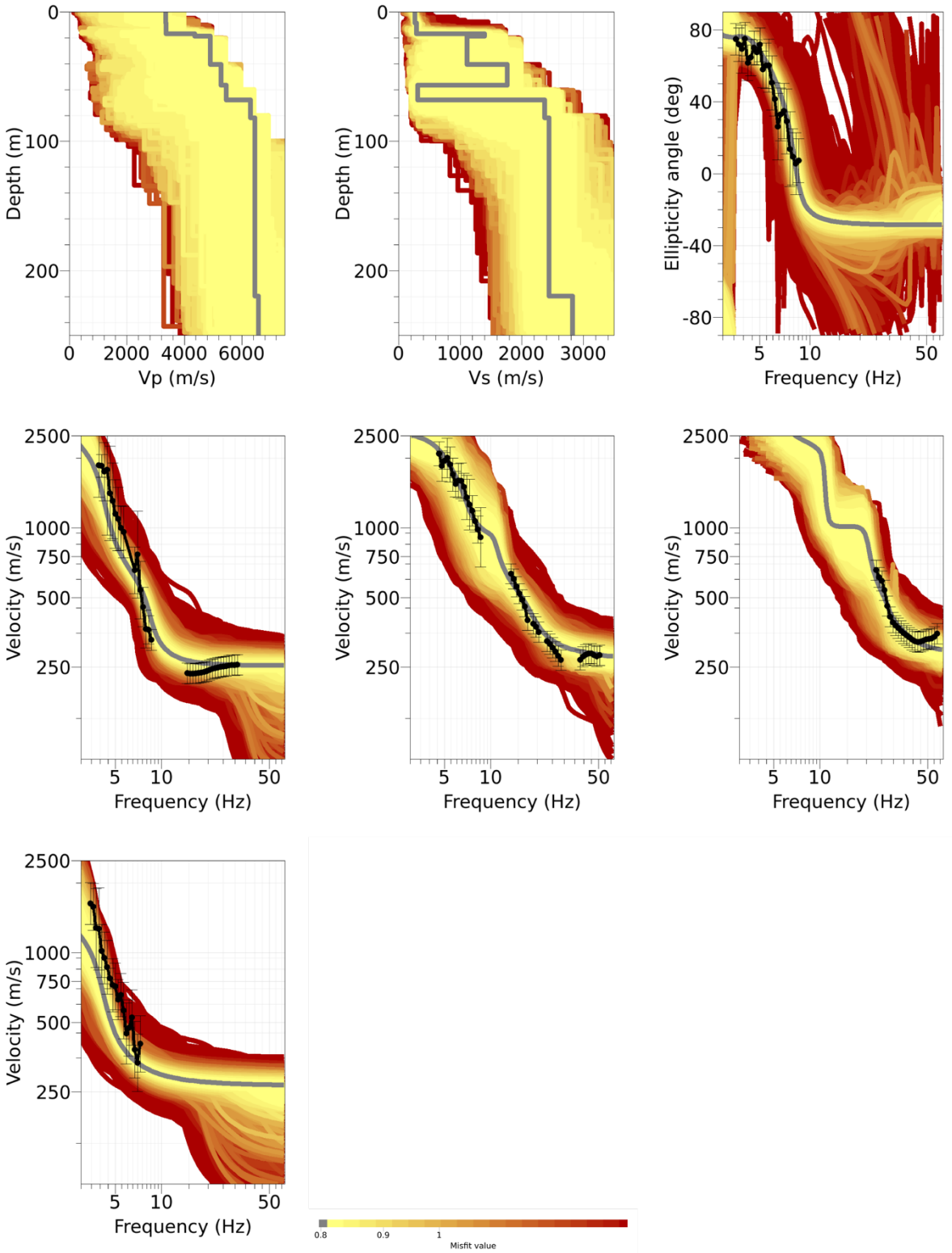

Figure 15*: Inversion SLUX 8l. Top row: P- (left) and S- (center) wave velocity profiles and ellipticity angle (right). Middle row: fundamental mode (left), first higher mode (center) and second higher mode (right) for the Rayleigh-wave dispersion curves. Bottom row: fundamental mode for the Love-wave dispersion curves. The black dots indicate the data points used for the inversion, the black bars the standard deviation of the inverted curve, while the gray line shows the best-fitting model.*

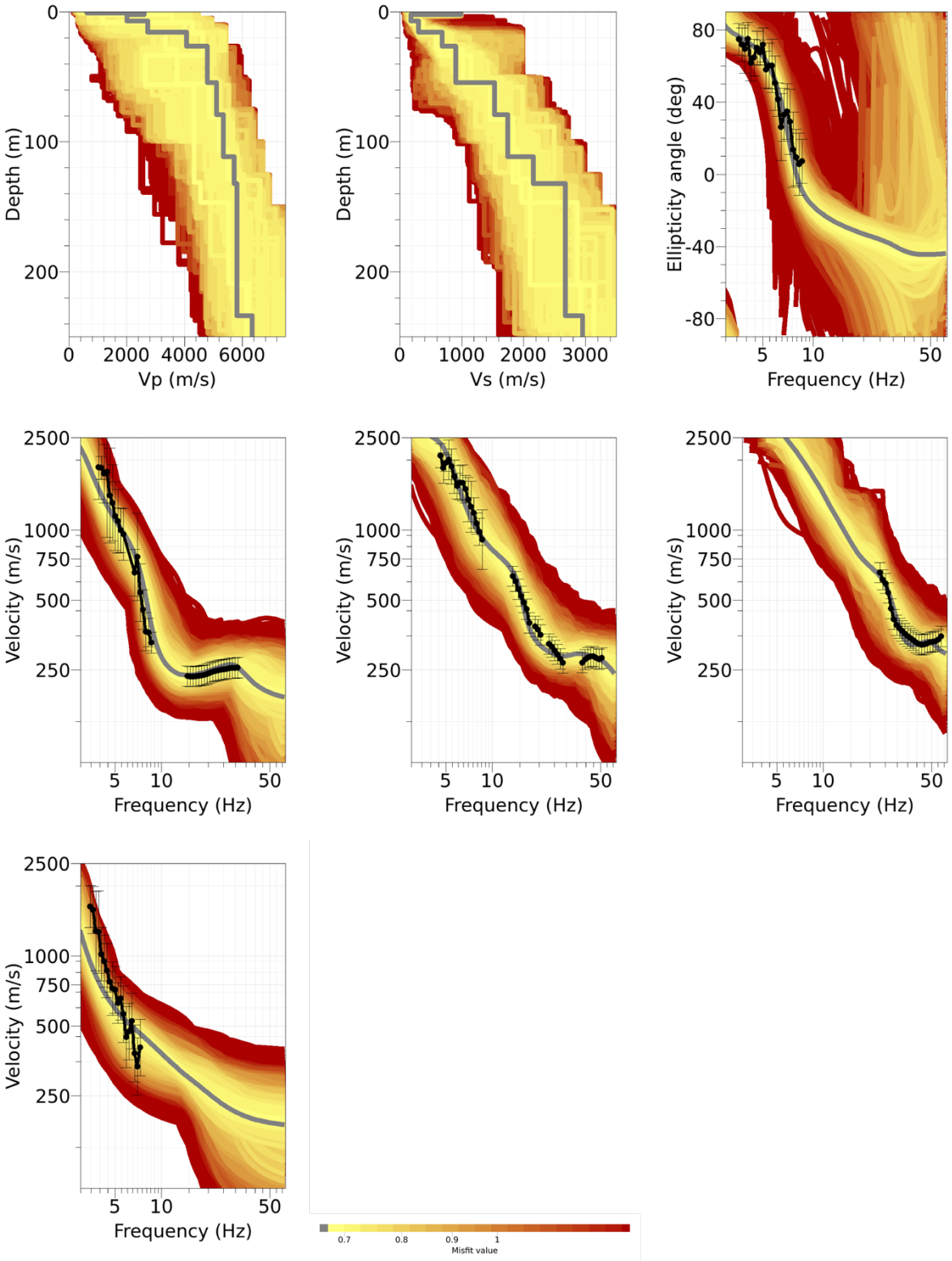

***Figure 16**: SLUX 10l. Top row: P- (left) and S- (center) wave velocity profiles and ellipticity angle (right). Middle row: fundamental mode (left), first higher mode (center) and second higher mode (right) for the Rayleigh-wave dispersion curves. Bottom row: fundamental mode for the Love-wave dispersion curves. The black dots indicate the data points used for the inversion, the black bars the standard deviation of the inverted curve, while the gray line shows the best-fitting model.*

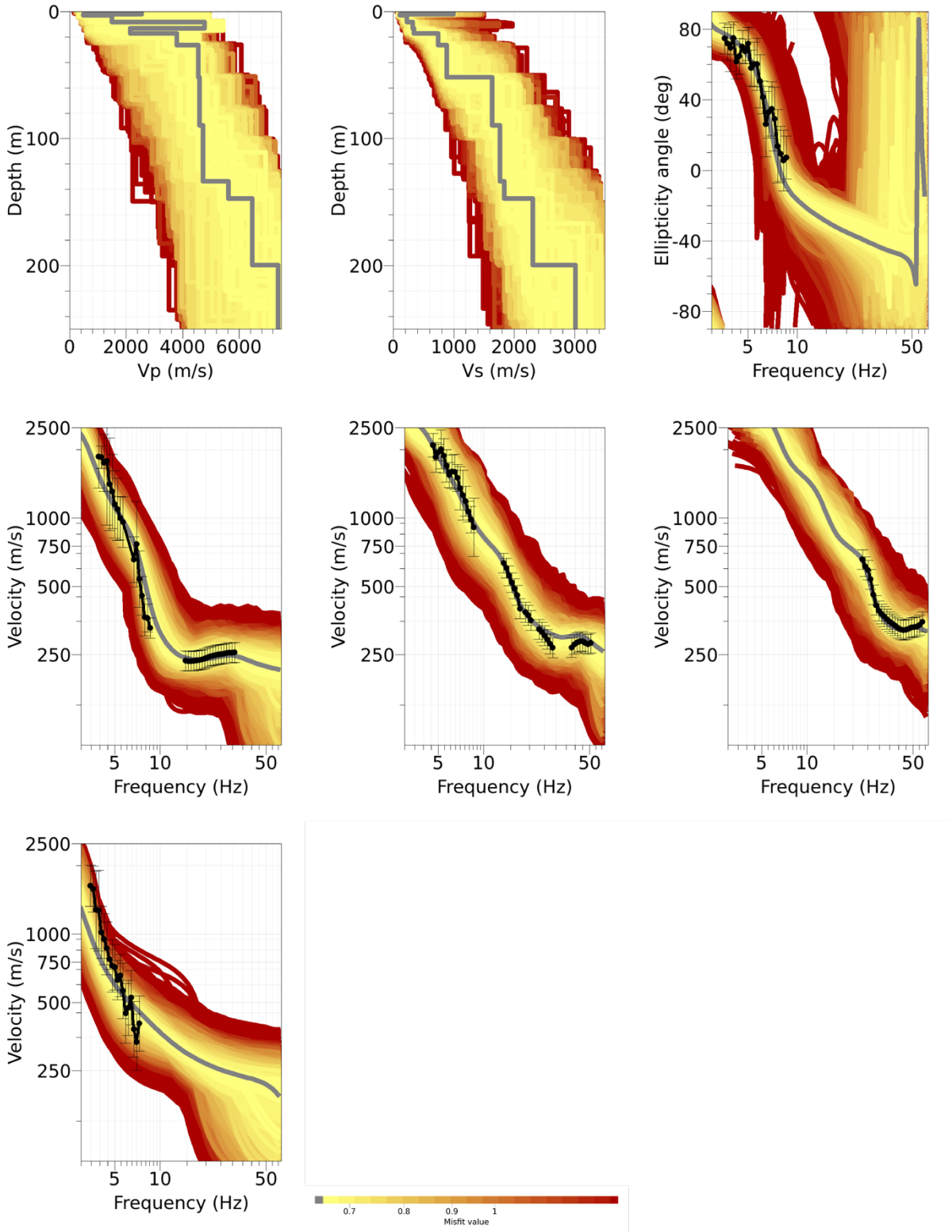

***Figure 17**: Inversion SLUX 12l. Top row: P- (left) and S- (center) wave velocity profiles and ellipticity angle (right). Middle row: fundamental mode (left), first higher mode (center) and second higher mode (right) for the Rayleigh-wave dispersion curves. Bottom row: fundamental mode for the Love-wave dispersion curves. The black dots indicate the data points used for the inversion, the black bars the standard deviation of the inverted curve, while the gray line shows the best-fitting model.*

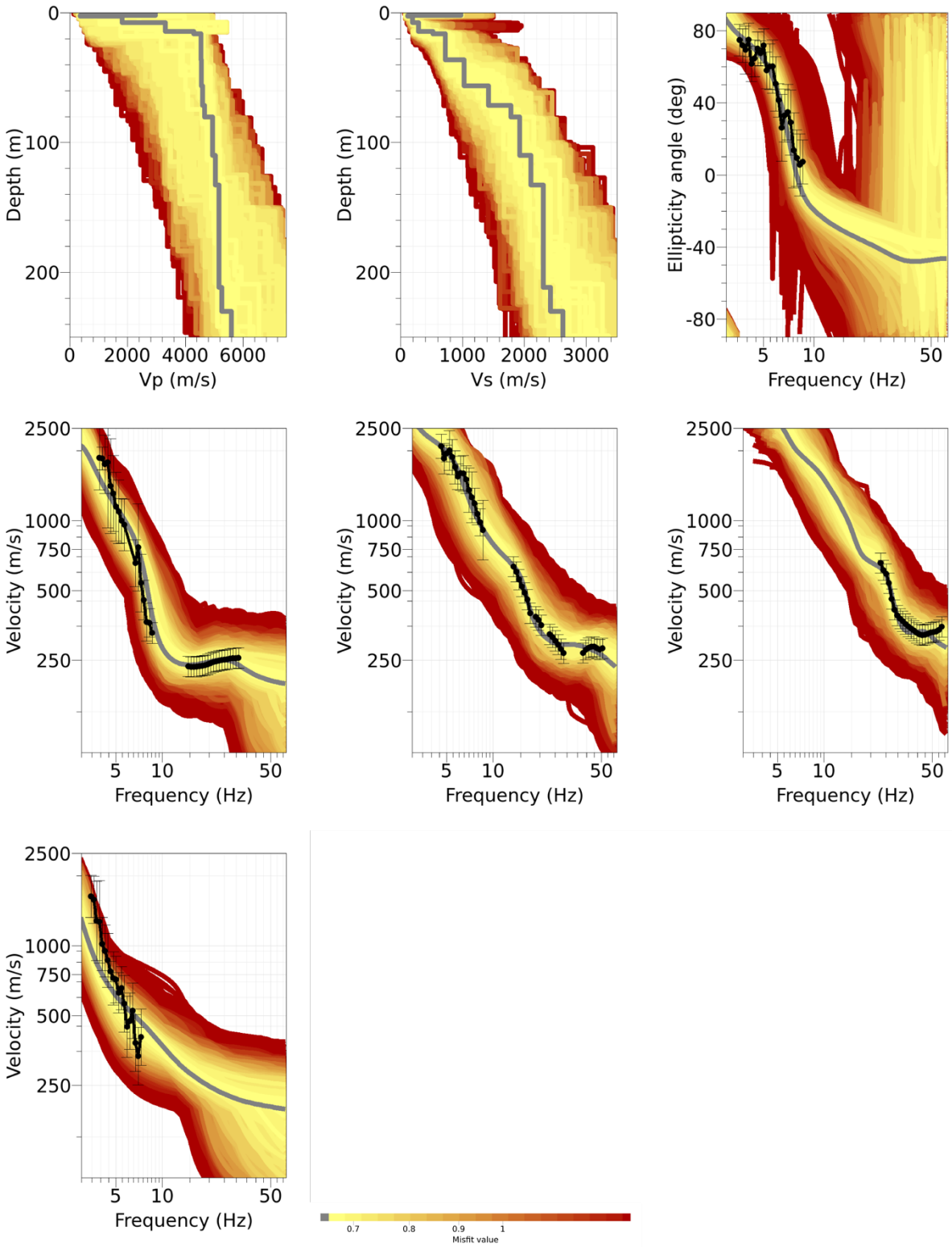

***Figure 18**: Inversion SLUX 14l. Top row: P- (left) and S- (center) wave velocity profiles and ellipticity angle (right). Middle row: fundamental mode (left), first higher mode (center) and second higher mode (right) for the Rayleigh-wave dispersion curves. Bottom row: fundamental mode for the Love-wave dispersion curves. The black dots indicate the data points used for the inversion, the black bars the standard deviation of the inverted curve, while the gray line shows the best-fitting model.*

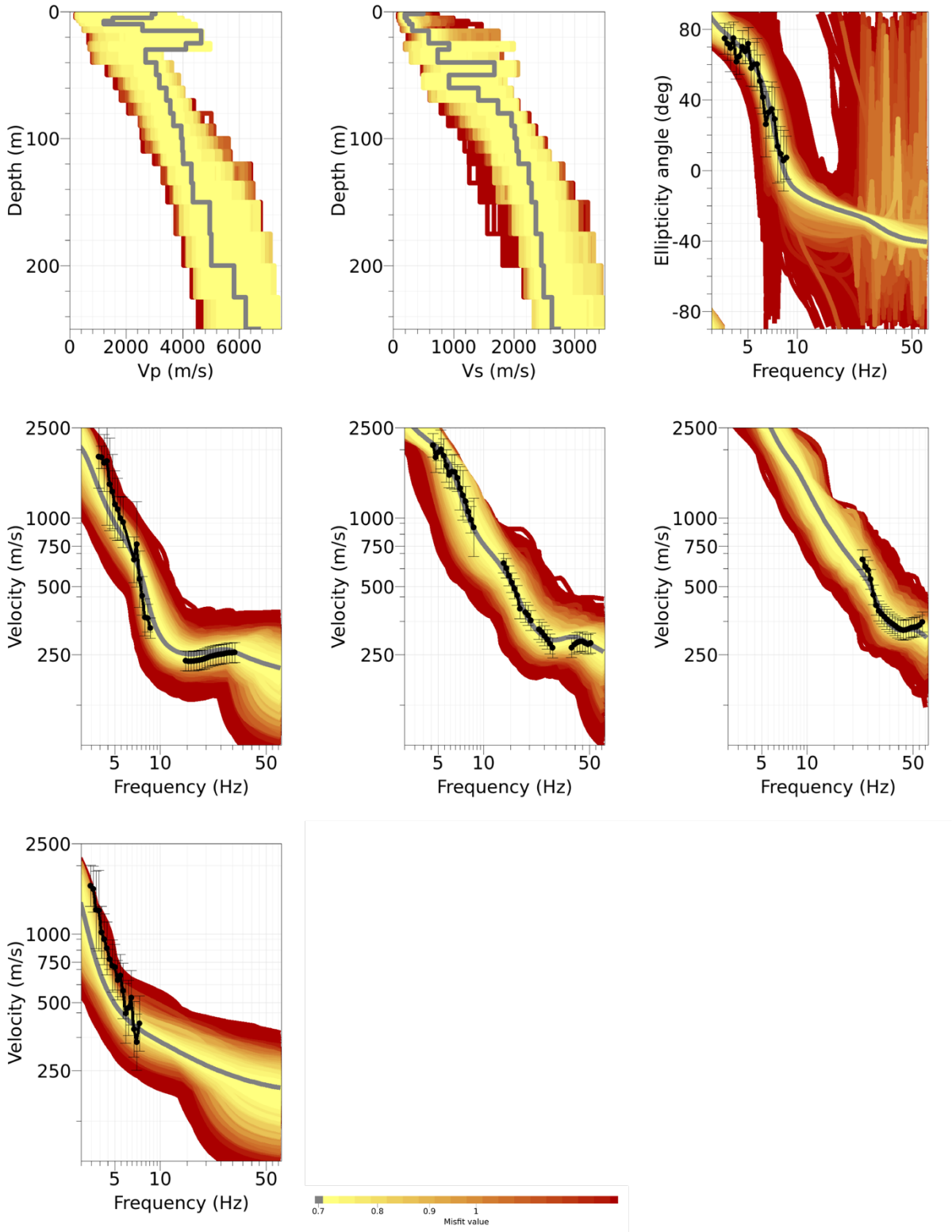

***Figure 19**: Inversion SLUX fix. Top row: P- (left) and S- (center) wave velocity profiles and ellipticity angle (right). Middle row: fundamental mode (left), first higher mode (center) and second higher mode (right) for the Rayleigh-wave dispersion curves. Bottom row: fundamental mode for the Love-wave dispersion curves. The black dots indicate the data points used for the inversion, the black bars the standard deviation of the inverted curve, while the gray line shows the best-fitting model.*

5.5 Inversion results - Neopsy

In addition to the five inversions performed using the *dinver* routine, the inversion was performed using the multizonal transdimentional Bayesian formulation (Neopsy – Hallo et al. 2021). The targets of the inversion are the fundamental, the first and the second higher modes of Rayleigh-wave dispersion curves and the fundamental mode of Rayleigh-wave ellipticity angle curve. The parametrization for the seismic velocities, density, Poisson's ratio and depth is defined within ranges: the S- and P-wave velocities range from 50 to 3500 m/s and from 100 to 7500 m/s, respectively, the density adjusts between 2000 and 3000 kg/m^3, while the Poisson's ratio is set to change between 0.2 and 0.45. The maximum depth is set to 250 m and the velocity inversion is allowed in the first 25 m. The inversion produced 5000 initial models and 25000 new models for a total of 30000 models.

The results of the inversion are shown in Fig. 20; the corresponding posterior marginal Probability Density Functions (PDF) for v_p, v_s, ρ and υ are shown in Fig. 21. The blue profile shows the results for the best model using the Maximum Likelihood (ML), while the magenta profile represents the model with the Maximum A Posteriori (MAP) probability.

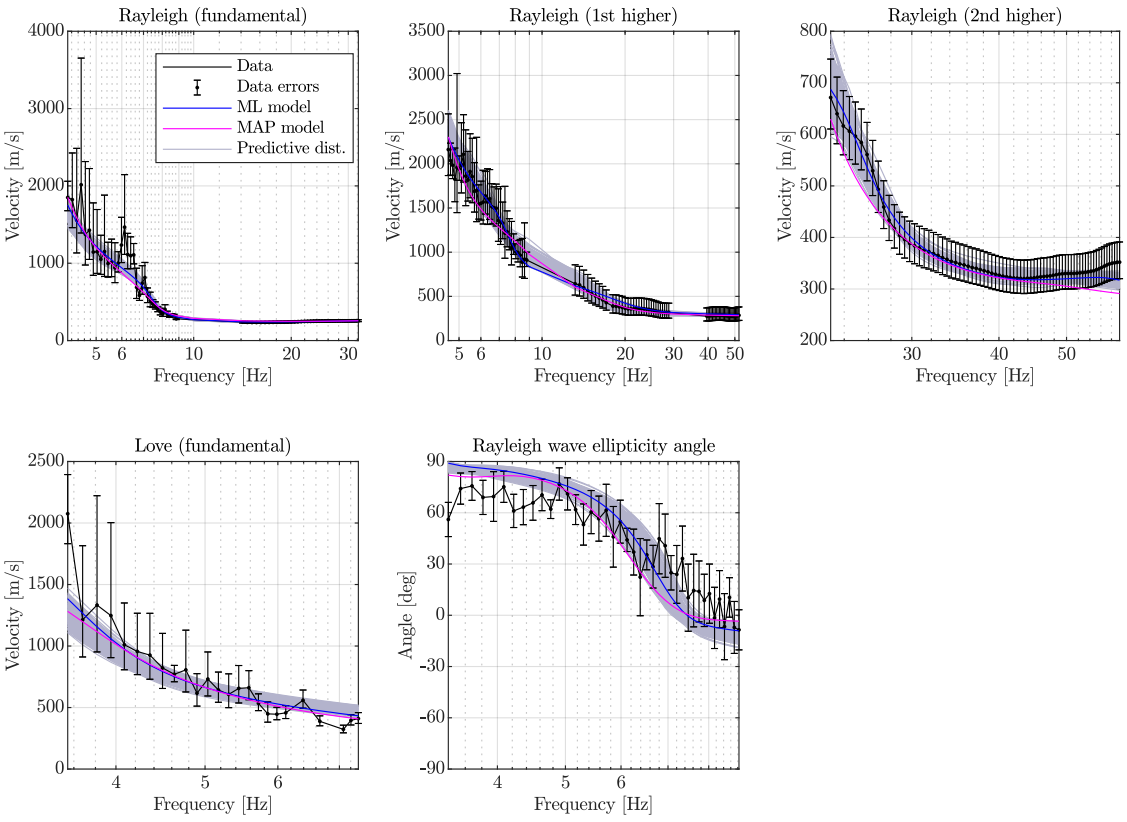

***Figure 20**: Results for the inversion using multizonal transdimensional Bayesian formulation. Top row: Rayleigh-wave fundamental mode, first and second higher mode. Bottom row: Love-wave fundamental mode and Rayleigh-wave ellipticity angle curve.*

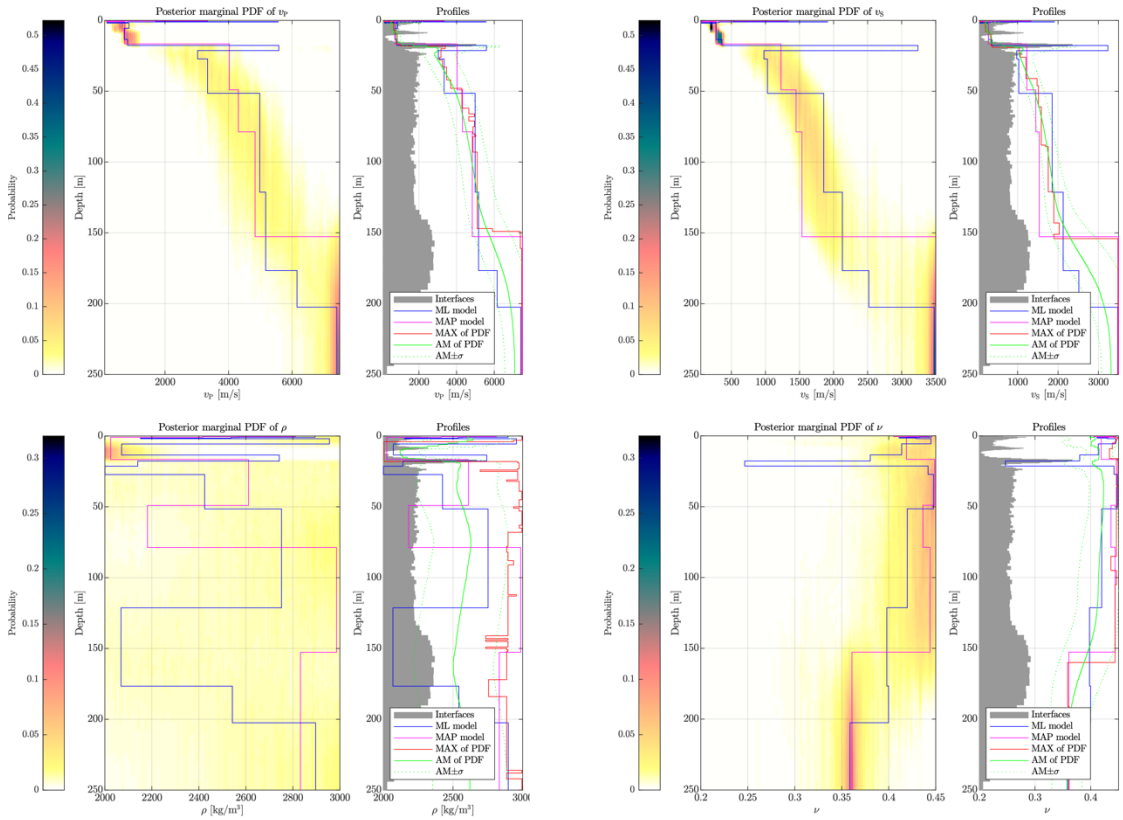

***Figure 21**: Posterior marginal PDF and profiles of P-waves (top left), S-waves (top right), density (bottom left) and Poisson's ratio (bottom right). Overview of the best profiles for each PDF for the Maximum Likelihood model (ML - blue) and the Maximum A Posteriori model (MAP - magenta).*

5.6 Discussion of the inversion results

The best-fitting models from each inversion are shown in Fig. 22: the S-wave velocity profiles investigating the subsurface down to 250 m (left) and a zoom into the first 30 m (right). The velocity profiles in green and the one in gray are the results of *dinver*, while the blue and the magenta models correspond to the velocity profiles with the lowest misfit of *Neopsy* for ML and MAP, respectively.

In the first 30 m, the *dinver* velocity profiles show a thin layer (around 1 m) with S-wave velocities of about 1000 m/s followed by a low-velocity zone down to 15 m and *Vs* of about 700 m/s. The *SLUX8l* velocity profile, with 8 layers over the half-space, has a first layer of 17 m and S-wave velocity of 265-270 m/s. A thin layer of 3 m with strong S-wave velocity contrast is followed by a decrease of velocity down to 1111 m/s.

At higher depths, the velocity profiles show a gradient with depth. One interface common to most of the velocity models can be distinguished at 50 m with shear-wave velocities between 1411 and 1633 m/s. The fix layers model (*SLUXfix*), in addition to the velocity contrast, present a low-velocity zone ending at about 60 m. Also the *SLUX8l* model show a velocity inversion between 56 and 68 m with a decrease in S-wave velocity to about 310 m/s. At 68 m the *Vs* of *SLUX8l* increases to 2376 m/s.

Several others independent interfaces can be distinguished for all models down to 250 m: e.g., at 132 m for the *SLUX10l* and at 147 m for the *SLUX12l*. The half-space of all these models is located

in a restricted zone between 200 m (*SLUX12l*) and 233 m (*SLUX10l*). With the exception of *SLUX14l*, where the S-wave velocity for the half-space increases from 2306 to 3017 m/s, all the other models present a much smaller velocity contrast.
The velocity profiles resulting from the different inversions have V_{S30} between 364.9 and 413.2 m/s, with an average value of 380.54 ± 19.49 m/s. The upper range of the V_{s30} values is linked to the *SLUX8l* model and to the low resolution of the shallow layers.
The results of Neopsy are shown for the ML (blue) and MAP (magenta) models. Generally, the MAP model is preferred because it represents the distribution of models. The ML profile shows a thin layer of 20 cm at a depth of 1 m with shear-wave velocity of more than 1900 m/s. Immediately below, a low-velocity zone (LVZ) takes place between 3 and 18 m with *Vs* of 273 m/s. A strong velocity contrast and shear-wave velocities up to 3250 m /s mark the end of the LVZ. Such high velocity is however considered rather unrealistic. This layer with a thickness less than 4 m covers a second velocity inversion extending down to about 50 m and velocity of 1854 m/s. The velocity profiles show a linear gradient down to the half-space. The half-space, in agreement with the results of *SLUX12l*, is located at about 200 m and has shear-wave velocities close to 3500 m/s. The MAP model, after the first shallow layer of 50 cm of thickness and *Vs* of 1333 m/s, shows a LVZ down to 16.6 m in agreement with all the other results. At around 17 m the shear-wave velocity increases to 1227 m/s. Due to the low number of layers in the MAP model, this profile shows an interface at 49 m in agreement with the other results. The half-space corresponds to a strong velocity contrast (about 3500 m/s) and is located at 152 m.
The V_{s30} for the MAP model is 392.56 m/s, while the V_{s30} for the ML is equal to 409.13 m/s. These values are slightly higher than the results of *dinver* inversion but still in agreement.

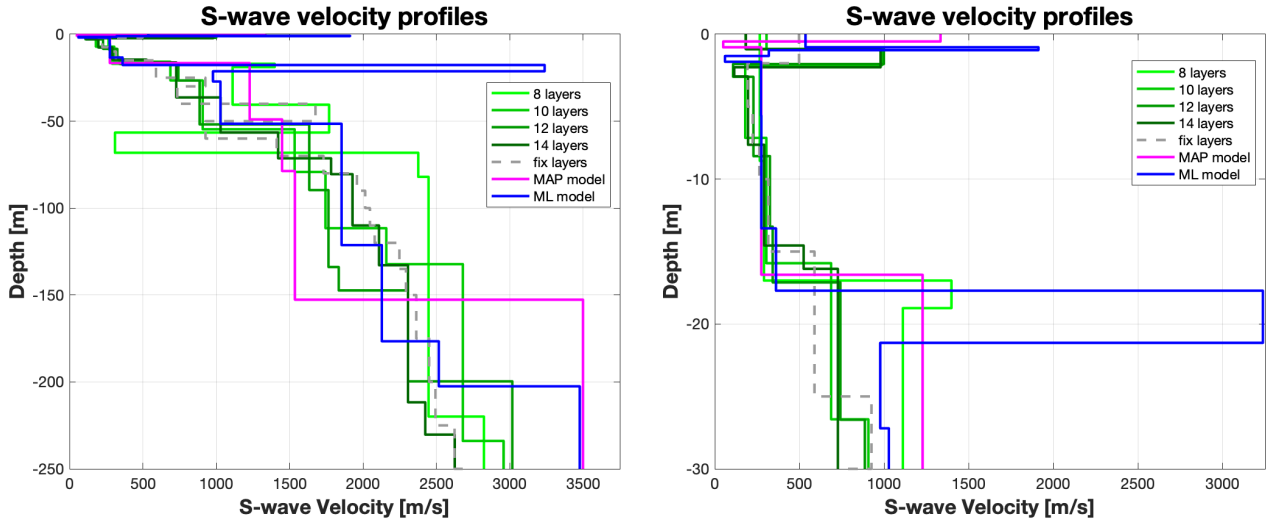

***Figure 22**: Overview of the best shear-wave velocity profiles of the different inversions (left) and zoom into the upper 30 m.*

6 Further results from the inverted profiles

6.1 SH transfer function

Figure 23 shows the SH-wave transfer functions, and the standard deviation curves, for the best velocity models of *dinver* analysis (black), for the ML (blue) and MAP (magenta) models from

Neopsy, and the empirical amplification function curve for the SLUX station (red). The present (21.09.22) empirical amplification function curve was computed for the strong motion sensor using a maximum of only 7 earthquakes in the frequency range: 1.42-15.03 Hz decreasing to 2 at 0.5 Hz and at 28.32 Hz. The shape of the empirical amplification curve shows an asymmetric peak at 4.7 Hz with amplitudes of 4.4. The left flank is long and less inclined than the right one, which is shorter. The amplification values above 6.3 Hz and below 1 Hz are close to 1.
The SH-wave transfer function for the best models of *dinver* inversion presents a broad peak at 4 Hz and amplifications of 4.36. Two smaller and sharp peaks can be seen at 11.1 Hz and at 18.9 Hz. These two peaks are comparable with the peaks in the empirical amplification curve, while for the one at lower frequency that similarity is smaller in terms of both shape and values over the frequency range 0.7-7 Hz. The transfer functions for Neopsy models overlap the curve for *dinver* model for frequencies below 3 Hz. Instead of a broad peak, the Neopsy SH-wave transfer functions have a narrow peak at 4.35 and 3.95 Hz, respectively, and a trough. At higher frequenciess the ML curve in blue is close to *dinver* results, while the MAP curve presents three sharp peaks at 11.2, 15.5 and 22.2 Hz. With respect to the empirical amplification function curve, both Neopsy SH-wave curves have generally higher amplification values.

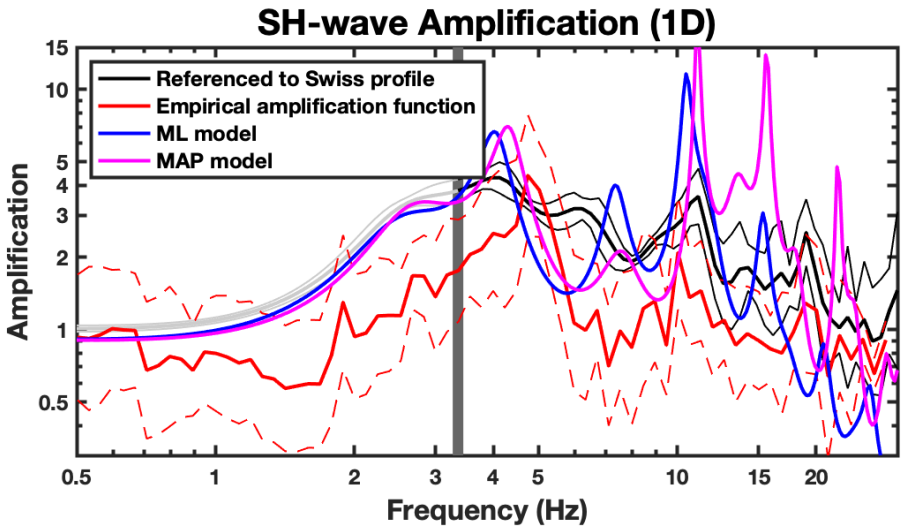

***Figure 23**: Modeled amplification function and standard deviation curves for the dinver profiles (black lines). Blue and magenta curves show the modeled amplification functions for the Maximum Likelihood and Maximum A Posteriori models for Neopsy inversion, respectively. All modeled curves are referenced to the Swiss rock profile. Red curves represent the empirical amplification (solid line) and its standard deviation (dashed lines) function at the SLUX station.*

6.2 Quarter-wavelength representation

The quarter-wavelength velocity approach (Joyner et al., 1981) provides, for a given frequency, the average velocity at a depth corresponding to 1/4 of the wavelength of interest. Figure 24 shows the quarter-wavelength results for the best velocity models of *dinver* inversions using the fundamental modes of Rayleigh- and Love- wave dispersion curves, the first and the second higher modes for the Rayleigh waves and the Rayleigh-wave ellipticity angle curve. The results using this proxy, considering frequency limits of the experimental data between 3.4 and 59.6 Hz for the dispersion curves and between 3.4 and 8.8 Hz for the ellipticity curve, is well constrained only to 24 m. The quarter-wavelength impedance contrast introduced by Poggi et al. (2012) is also

displayed in the figure. It corresponds to the ratio between two quarter-wavelength average velocities, respectively from the top and the bottom part of the velocity profile, at a given frequency.

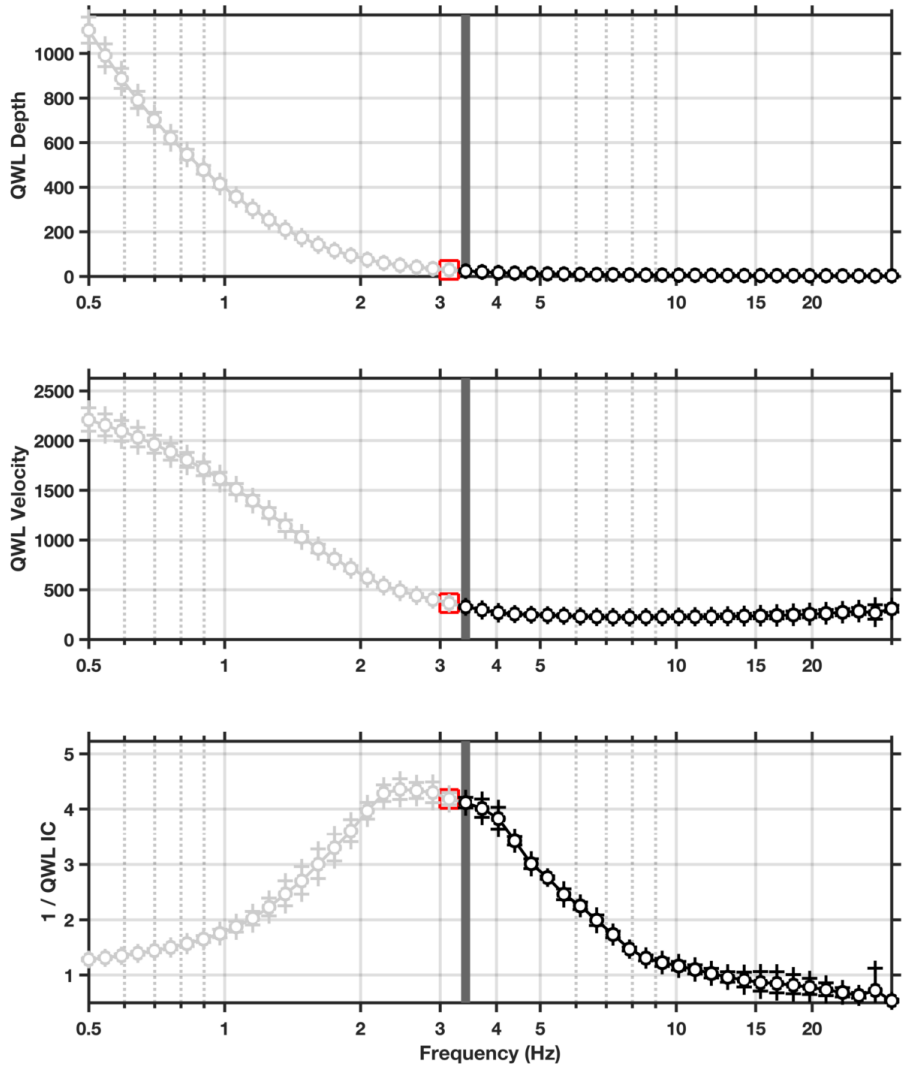

***Figure 24**: Quarter wavelength representation of the velocity profiles for the best models of the inversions (top: depth, center: velocity, bottom: impedance contrast). The light and dark grey bars overlapping show the ellipticity lower frequency value and the lower frequency value obtained with dispersion curves, respectively. Red square corresponds to f_{30} (frequency related to the depth of 30 m).*

7 Discussion and conclusions

The passive array measurement and the MASW acquisition performed in August 2021 allowed the investigation of the near subsurface underneath the SLUX station. The study area is located south-west of the village of Vignogn (GR) on the western side of Lumnezia valley. From the geological

point of view, the site is located on an active landslide moving towards the river Glogn between 1 and 20 cm per year.
The H/V analysis identified a central area rather homogeneous with H/V curves consisting in a broad and rather flat f_0 peak at 2.5-5.7 Hz and a narrow trough (7.8 Hz) whose values are lower than 1. Towards south-west and north, the H/V peak shifts to higher frequencies.
The data processing performed for the passive seismic array allowed the identification of Love- and Rayleigh-wave dispersion curves and Rayleigh-wave ellipticity curves. The MASW acquisition allowed the picking of Rayleigh-wave dispersion curves using the vertical and radial components of seismic motion. The picked dispersion curves and the ellipticity angle curve were inverted for the estimation of P- and S-wave velocity profiles down to 250 m.
Five similar velocity profiles were estimated using *dinver* and two (ML and MAP) using Neopsy technique. The parametrizations chosen for the *dinver* inversion have between 8 and 14 layers over the half-space. With the exception of the *SLUX8l* model, the four remaining models present similar features: a shallow layer with high shear-wave velocities of 1000 m/s, a low velocity zone down to 15 m and a second velocity contrast at 50 m with an increase of velocity up to 1633 m/s. At higher depths these velocity models show a velocity gradient with depth. The half-space is located between 200 and 233 m and does not present any strong velocity contrast. The only exception is the half-space for *SLUX12l* model where the *Vs* increases from 2306 to more than 3000 m/s. *SLUX8l* model has lower resolution and does not resolve the shallow low-velocity zone and locates a strong velocity contrast at 17 m. The model with layers at fix depth has a trend which is similar to most of the *dinver* velocity profiles. Above and below the interface at 50 m, this model presents two velocity zones.
The results of Neopsy are similar to that of *dinver* inversion in the first 50 m. The ML and MAP models present a fast layer in the shallowest meters, a low-velocity zone down to about 16 m and an additional velocity contrast at around 50 m. Generally, the MAP model is preferred because it better represents the distribution of velocity profiles. At higher depths the MAP model, probably due to the lower number of layers, shows a shallow half-space at about 152 m with a strong velocity contrast (*Vs*=3500 m/s). The ML model presents a second velocity inversion between the interface at 16 and 50 m and a linear gradient with depth down to 200 m, at the half-space. The high velocities above the low-velocity zones in the ML profile have to be interpreted with caution, because they often show rather unrealistic values.
The V_{S30} value for the best velocity model of *SLUX10l* model is 373.65 m/s; it corresponds to soil class B in EuroCode (EC8) and C in Swiss building code (SIA261).
The empirical amplification function curve for the SLUX strong motion has an asymmetric peak at 4.4 Hz. At low and high frequencies, the ESM curve is rather flat with values close to 1. The SH-wave transfer functions for the models of *dinver* and Neopsy have higher amplification values over the entire frequency range. Around the ESM peak the *dinver* SH-wave curve has a broad peak, while the two curves of Neopsy have the left flank of a broad peak evolving into a small peak at about 4 Hz and amplifications up to 5 and a trough at 5-6 Hz.

References

Burjánek, J., Gassner-Stamm, G., Poggi, V., Moore, J. R., and Fäh, D. (2010). Ambient vibration analysis of an unstable mountain slope. Geophys. J. Int., 180:820–828.

Burjánek, J., Moore, J. R., Molina, F. X. Y., and Fäh, D. (2012). Instrumental evidence of normal mode rock slope vibration. Geophys. J. Int., 188:559–569.

Fäh, D., Gardini, D., et al. (2003). Earthquake Cataloque of Switzerland (ECOS) and the related macroseismic database. Eclogae geol. Helv. 96.

Fäh, D., Wathelet, M., Kristekova, M., Havenith, H., Endrun, B., Stamm, G., Poggi, V., Burjanek, J., and Cornou, C. (2009). Using ellipticity information for site characterisation. NERIES deliverable JRA4 D4, available at http://www.neries-eu.org.

Fritsche, S., Fäh, D., Gisler, M., and Giardini, D. (2006). Reconstructing the damage field of the 1855 earthquake inSwitzerland: historical investigations on a well-documented event Geophys. J. Int. (2006)166, 719–731

Hobiger, M., Bard, P.-Y., Cornou, C., and Le Bihan, N. (2009). Single station determination of Rayleigh wave ellipticity by using the random decrement technique (RayDec). Geophys. Res. Lett., 36.

Maranò, S., Reller, C., Loeliger, H.-A., and Fäh, D. (2012). Seismic waves estimation and wavefield decomposition: Application to ambient vibrations. Geophys. J. Int., 191:175–188.

Poggi, V. and Fäh, D. (2010). Estimating Rayleigh wave particle motion from three component array analysis of ambient vibrations. Geophys. J. Int., 180:251–267.

Poggi, V., Edwards, B., and Fäh, D. (2010). Characterizing the Vertical-to-Horizontal Ratio of Ground Motion at Soft-Sediment Sites. Bulletin of the Seismological Society of America, 102(6): 2741 2756.

Socco, L. V., D. Boiero, S. Foti, and R. Wisén (2009), Laterally constrained inversion of ground roll from seismic reflection records, *Geophysics*, *74*(6), G35-G45, doi:10.1190/1.3223636.

Socco, L. V., and C. Strobbia (2004), Surface-wave method for near-surface characterization: a tutorial, *Near Surface Geophysics*, *2*(4), 165-185, doi:https://doi.org/10.3997/1873-0604.2004015.

Wathelet, M., Chatelain, L., Cornou, C., Giulio, G. D., Guillier, B., Ohrnberger, M., and Savvaidis, A., 2020. Geopsy: A User-Friendly Open-Source Tool Set for Ambient Vibration Processing, *Seismological Research Letters*, XX, 1–12.